MEASURING RE-ENTRY AEROHEATING OF SATELLITE COMPONENTS AT TRUE FLIGHT TOTAL ENTHALPIES

James Leader, Joseph Steer, Peter Collen and Matthew McGilvray

Oxford Thermofluids Institute, Southwell Building, University of Oxford, Oxford OX2 0ES

ABSTRACT

At end-of-life, satellites are currently removed through uncontrolled re-entry into Earth's atmosphere. Ideally, satellite components 'burn up' due to aerothermal heating loads but Earth impact events are known to occur. Modelling of aerothermal heating at high altitudes is difficult due to the rarefied flow regime coupled with high temperature gas effects generated by entry speeds over 6 km/s. This study develops and demonstrates a test bed for heat flux measurements at high enthalpy, high altitude conditions. A rarefied flow condition is commissioned in the T6 expansion tunnel with a freestream Knudsen number of 0.011 and total enthalpy in the range 19-22 MJ/kg. Flat-faced cylindrical models are used to represent satellite tanks. The models are instrumented with platinum thin film heat transfer gauges to obtain spatially resolved heat flux measurements and coated in a silicon dioxide film to insulate them from free electrons in the ionised flow. Post-shock conditions are matched to those expected in flight at altitudes in the range 81-90 km.

***Index Terms*—** expansion tunnel, satellite demise, heat transfer, thin film gauge

1. INTRODUCTION

Defunct satellites are currently de-orbited to comply with guidelines laid out by the Inter-Agency Space Debris Coordination Committee (IADC) [1]. Disposal by direct re-entry into Earth's atmosphere is preferred. These guidelines are intended to prevent over-crowding of the Low Earth Orbit (LEO) region, which has accumulated a significant amount of orbital debris since the advent of the space age. Table 1 presents current estimates for the debris object inventory, with most of these debris items intersecting the LEO region. Without positive action to limit the amount of orbital debris, collisions and fragmentations could lead to an uncontrollably growing debris belt [2].

Aerothermal heating during re-entry causes de-orbited satellites to burn up in the Earth's atmosphere. Satellites can be reduced to negligible mass, hence the preference for this disposal method. Occasionally, re-entering bodies fail to burn up completely leading to Earth impact events. One such event occurred in 2001, when a 70 kg tank from a Payload Assist Module - Delta (PAM-D) rocket upper stage crashed into the Saudi Arabian desert. The stage had been orbiting Earth as a defunct satellite for eight years before re-entry and partial burn up. Thousands of other individual Earth impact events have been recorded [4].

Table 1: ESA estimate of the number of orbital debris items, by size [3].

Size of debris object	Est. number in orbit
> 10 cm	36,500
1 cm - 10 cm	1,000,000
1 mm - 1 cm	135 million

Computational models have been developed by space agencies and private corporations to predict re-entry trajectories and ground risk. These models are now in their third generation and can process complex break-up scenarios in three degrees of freedom [5]. However, accurate heat flux prediction in the rarefied slip-transition regime at high speeds is difficult. There is also a distinct lack of experimental data to verify and improve these models. Most of the re-entry literature focuses on aerodynamically simple geometries rather than complex bodies. Very few studies have gathered data at conditions replicating flight, particularly total enthalpy.

This paper demonstrates the suitability of the T6 Stalker Tunnel for experimentation at rarefied upper atmosphere re-entry flow conditions. It details the design and commissioning of a flight-equivalent test condition for simulation of re-entry at 6.0 - 6.5 km/s and 80-90 km altitude. Figure 1 defines the operational region for this study in relation to approximate operating capabilities.

Heat transfer data was gathered using subscale models instrumented with platinum thin film gauges (TFGs) to allow for spatially resolved measurements. A novel model mount was designed to allow for simultaneous multi-model testing and to avoid damage from particulates caused by operation of the tunnel. Results are presented for flat-faced cylinders in both an axial and crossflow orientation, with measurements at several spatial locations. These measurements are compared to numerical simulations performed using the open source Eilmer4 solver [7].

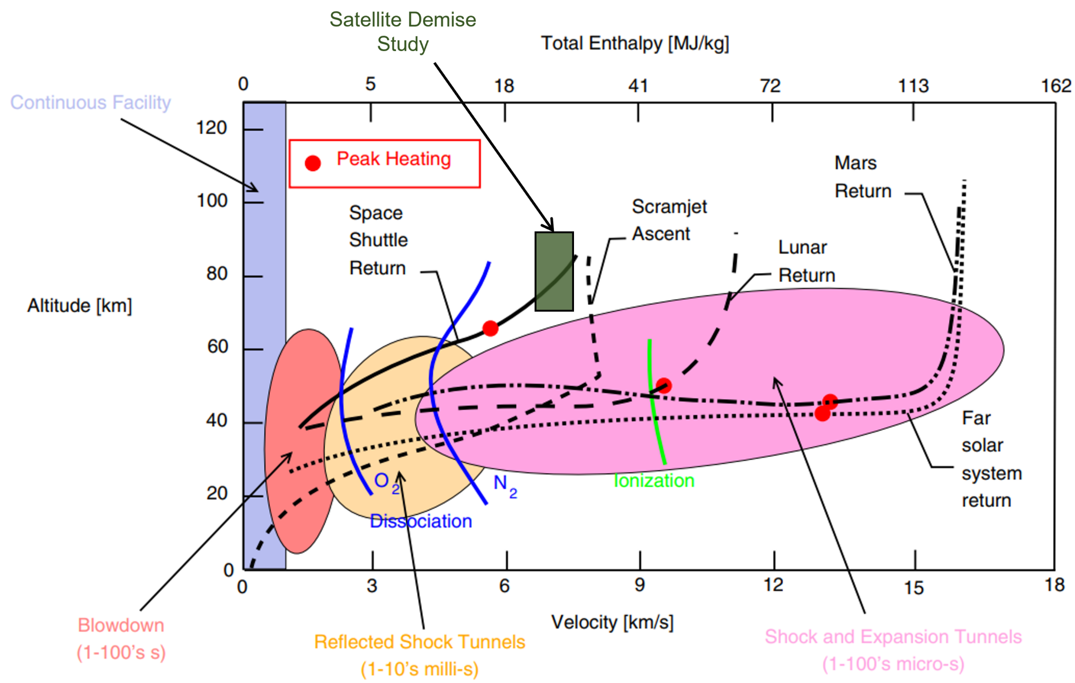

Fig. 1: Selected mission trajectories and approximate ground test facility capability regions, adapted from Fletcher [6]. The region of interest for this satellite demise study conducted in the T6 expansion tunnel is identified.

2. EXPERIMENTAL SETUP

The experiment aims to replicate the flight environment for re-entering cylindrical pressure vessels of 0.5 to 5 m in diameter, in the altitude range 70-90 km. Here, the flight velocity varies only marginally around the nominal LEO re-entry value of 7 km/s. To replicate conditions on the stagnation line, several experimental parameters must be matched to flight. These are the total enthalpy, gas composition and post-shock density-length scale product (post-shock ρL) [8]. The body length scale, L, is taken to be equal to the cylinder diameter. Matching post-shock ρL ensures critical non-dimensional parameters, such as Knudsen number and Reynolds number, are also matched in the shock layer. Figure 2 shows the calculated envelope of post-shock ρL values for re-entry at 7 km/s, providing a target for matching.

The flight-equivalent velocity, U_{eq}, is defined by Eq. (1), where h_0 is the total specific enthalpy. Flight-equivalent velocity is used in place of total enthalpy in the discussion of matching. The target value for U_{eq} in this study is 7 km/s.

$$h_0 = h + \frac{1}{2}U^2 = \frac{1}{2}U_{eq}^2 \tag{1}$$

Without matching freestream Mach number, measurements obtained after expansion of the shocked gas (i.e. on a side face) cannot be directly extrapolated to flight. However, these measurements are still useful in validation of numerical codes as simulations can be run with the same freestream properties as the experiment, giving complete equivalence. Heat transfer measurements at a single post-shock ρL value can be used to validate simulations across a range of flow conditions as the body length scale can be changed to ensure post-shock ρL is conserved. As such, conducting experiments across a range of post-shock ρL values should provide useful data for a wide range of conditions.

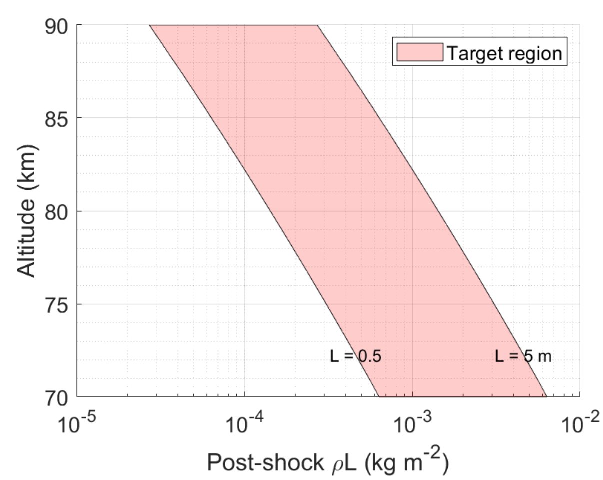

Fig. 2: Envelope of post-shock ρL expected in flight for satellite demise at 7 km/s.

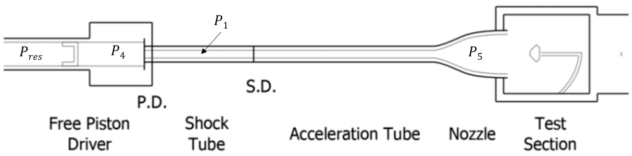

Fig. 3: Simplified schematic of the T6 expansion tunnel at primary diaphragm rupture, adapted from [11].

2.1. Condition development

The T6 Stalker tunnel is a multi-mode hypersonic wind tunnel located at the University of Oxford [9]. The free-piston driver may be coupled to a range of downstream components to allow operation of the facility as either a shock tube, expansion tube, expansion tunnel, or reflected shock tunnel. Experiments performed during this study used the expansion tunnel mode with a new Mach 10 nozzle coupled to the end of the expansion tube [10]. A simplified facility schematic is shown in Figure 3.

To produce a rarefied flow condition, the 'low' driver condition with the lightweight piston was selected. The performance map shown in Figure 4 was created using the in-house Oxford Equilibrium Code (OEC) which is a one-dimensional state-to-state solver that uses the CEA2 program [12] to evaluate state properties at thermochemical equilibrium. The tunnel configuration parameters that can be varied within the 'low condition' mode are the percentage of helium in the helium-argon driver gas (X_{He}) and the shock and acceleration tube fill pressures (P_1 and P_5, respectively). Increasing the proportion of helium in the driver gas, which fills the compression tube between the piston and primary diaphragm, leads to higher shock speeds and flight-equivalent velocities. To produce Figure 4, P_1 was varied between 500 and 1000 Pa and P_5 between 1 and 10 Pa. The OEC predicts that decreasing P_5 tends to increase flight-equivalent velocity but decreases post-shock ρL to unfavourably low values. The effect of altering P_1 was less clear. Figure 4 suggests that flight-relevant total enthalpies are achievable with a driver gas composition of 40 vol.% helium, but modification may be needed to increase post-shock ρL into the desired range.

Three condition shots were conducted in T6 to calibrate the OEC performance map and provide physical data on the proposed flow condition. Table 2 presents the tunnel configuration for each shot and gives the key results from post-processing of the flow condition data. Both the OEC prediction and the true experimental flow parameters from each condition shot have been added to Figure 4, demonstrating a tendency for the OEC to underestimate post-shock ρL.

The condition tests were conducted using nine radially spaced Pitot probes at 20 mm from nozzle exit. In each test, the shock and acceleration tube shock speeds were measured. These shock speeds were used within a second equilibrium state-to-state solver, PITOT [13], in 'experimental' mode to resolve the remaining flowfield parameters. The measured Pitot pressures were averaged over the identified test time and used to validate the PITOT code output.

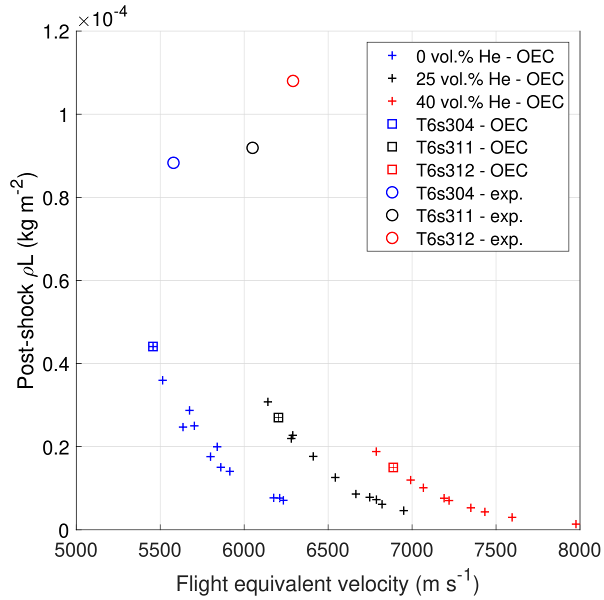

Fig. 4: T6 expansion tunnel performance map with the 'low' driver condition, produced using the state-to-state OEC solver. OEC predictions and experimental results from the condition shots are overlaid.

Table 2: Tunnel configuration parameters and condition data for the satellite demise condition shots. $P_1 = 1000$ Pa for each.

Shot	X_{He} (vol.%)	P_5 (Pa)	Kn_∞ -	U_{eq} (m s^{-1})	P-s ρL (kg m^{-2})
T6s304	0	10	0.012	5579	8.82x10^{-5}
T6s311	25	7.5	0.012	6050	9.19x10^{-5}
T6s312	40	7.4	0.011	6291	1.08x10^{-4}

The Pitot pressure traces for shot T6s312 are shown in Figure 5. The arrival of the accelerator gas can be clearly seen with a short period of flow establishment. The test gas slug then arrives and a quasi-steady test time can be identified from 200 to 300 µs. This is followed by the arrival of the unsteady expansion. Shot T6s312 saw a flight-equivalent velocity of 6300 m/s, approaching within 10% of the desired 7 km/s. Freestream Knudsen numbers above 0.01 demonstrate a rarefied flow condition well within the slip regime. Post-shock ρL values of approximately 10^{-4} kg/m^2 fall within the target envelope defined in Figure 2, indicating that post-shock conditions driving heat transfer are matched to flight. The T6s312 tunnel configuration was selected to generate the satellite demise flow condition used in heat flux testing.

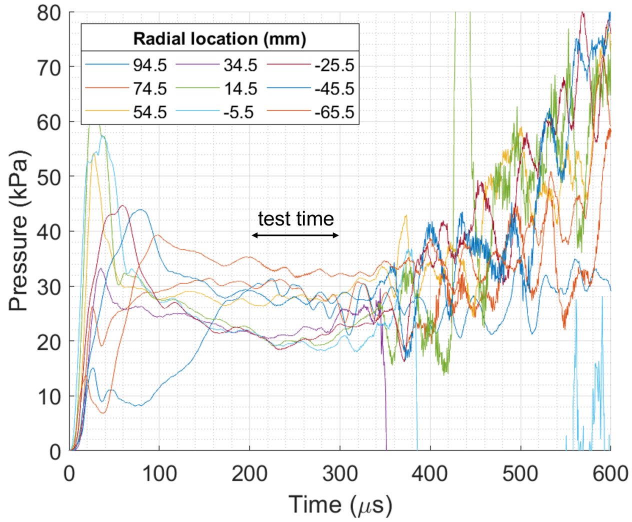

Fig. 5: Pitot probe pressure traces from shot T6s312, with a quasi-steady test time identified.

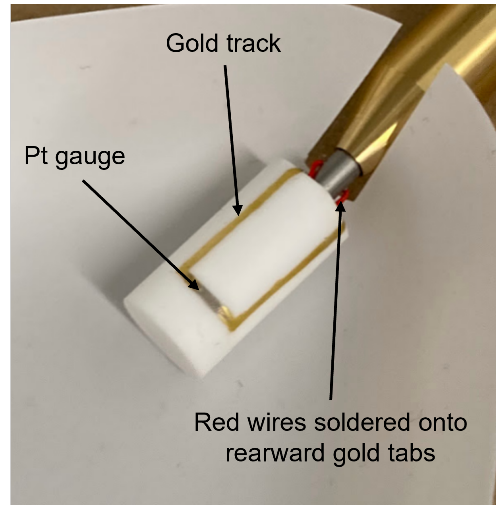

Fig. 6: An axial cylinder model instrumented with a platinum thin film gauge on the curved surface.

2.2. Subscale models and instrumentation

Flat-faced cylindrical models, representing pressure vessels, were chosen as the effect of the sharp-edged geometry on heat transfer is of particular interest. The models have a diameter of 10 mm, length of 20 mm and a 0.25 mm corner radius. These dimensions were selected to give a realistic aspect ratio, as determined from ESA's Database and Information System Characterising Objects in Space (DISCOS) [14]. Macor was specified as the material for the model body as it has desirable thermophysical properties and is relatively easy to machine. Axial models have the cylinder axis aligned with the flow while crossflow models have the cylinder axis perpendicular to the flow direction. Several of each model were produced to build a full picture of surface heat transfer in the two different orientations.

The models were instrumented with platinum TFGs, placed at a variety of spatial locations on the model body surface. Figure 6 shows an example of an axial cylinder model with the platinum gauge on the curved face. The gauge is approximately 2 mm in length, 0.3 mm in width and of the order 1 μm thick. Gold tracks carry the electrical signal across the surface of the Macor model to wires soldered onto two gold tabs. The gold tabs are located on the rearmost part of the model to keep them sheltered from the flow. TFGs are passive constant current devices. A change in temperature at the gauge causes its resistance to change, altering the voltage measured across the gauge. This leads to a linear temperature-resistance characteristic. In this study, a Lancaster heat transfer amplifier from ASH Wireless Electronics was used to regulate the current to the gauges. A National Instruments computer (DAQ) was used to control the triggering of the Lancaster unit.

The models were coated in a layer of silicon dioxide to insulate the gauges from electrons in the ionised flow. This was done after the models had been instrumented and assembled on brass holders. Silicon dioxide with a purity of 99.99% was evaporated onto the models using ebeam evaporation in a Leybold 560 box coater. The film thickness applied was in the range 700 to 800 nm, as used by Willeke and Bershader [15].

2.3. Model mounting

A multi-model mount was designed to hold up to 12 models and/or Pitot probes at a radial distance of 75 mm from the nozzle centreline. This allows multi-model testing with the models all at the same radius, eliminating the effect of radial variations in the flowfield. The mount also removes the models from the main debris field produced when the primary diaphragm ruptures, avoiding damage by the aluminium particles that are released. CAD of the ring-type model mount assembled on the T6 mounting arm is shown in Figure 7. The T6 traverse can be used to rotate the whole assembly by up to ± 20 degrees for testing at an angle of attack. The mount holds the models close to the centre of rotation of the traverse which prevents them from being pushed into the nozzle boundary layer when moved to a non-zero angle of attack.

The ring design blocks only a small proportion of the nozzle area meaning that the flow over the models is unaffected by the presence of the mount. The low blockage ratio can be seen in Figure 8. This photograph from the unsuccessful shot T6s333 also shows how the mount shields the sensor wires from the flow with protective channels that carry them into the hollow sting. In Figure 8, two of the twelve ring positions are in use: a crossflow model is mounted on the left of the image, and a Pitot probe at the top.

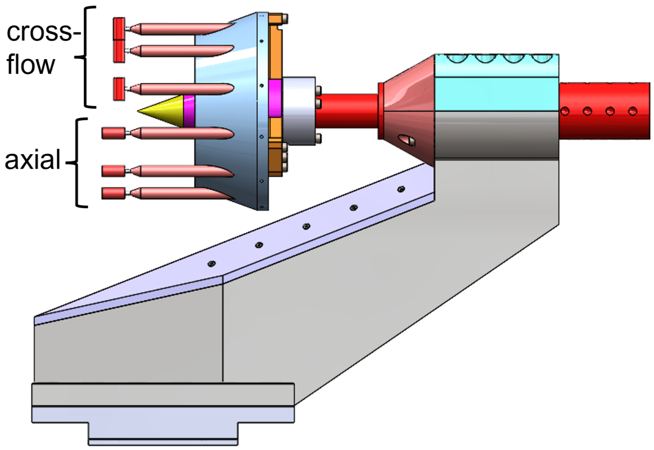

Fig. 7: CAD of the models and mount assembled on the T6 model mounting arm. The firing position shown allows the models to be positioned over the centre of rotation of the traverse.

Fig. 8: Photograph from shot T6s333 showing sensor wires taped into channels in the ring mount.

3. HEAT FLUX PREDICTIONS

3.1. Literature correlations

The Sutton-Graves [16] correlation for blunt body stagnation point heat flux is given by Eq. (2). It is valid in the total enthalpy range 2.3-116.2 MJ/kg and assumes equilibrium chemistry in the shock layer. K = 0.113 kgs^{-1}m$^{-3/2}$atm$^{-1/2}$ for air.

$$q_s = K\sqrt{\frac{p_0}{R_{eff}}}\,(h_0 - h_{wall}) \tag{2}$$

For the axial cylinder case, the relationship R/R_{eff} = 0.29 was obtained from Zoby and Sullivan [17], while an additional factor of $\sqrt{2}$ was included to account for the non-axisymmetric geometry in the crossflow case. The chemical equilibrium assumption implies that dissociated shock layer gas releases stored chemical energy in the boundary layer, as it approaches the cold wall. As such, the equilibrium assumption represents an upper bound estimate for the stagnation point heat flux. The opposing assumption is that the shock layer is in a ‘frozen’ state, whereby the gas composition does not change across the shock. Chemical energy is therefore not released as the gases cool in the boundary layer. To calculate the stagnation point heat fluxes using the frozen gas assumption, the total enthalpy h_0 must be replaced by the frozen gas recovery enthalpy [18]. The resulting estimates for stagnation point heat flux, using flow variables from shot T6s312, are presented in Table 3. In reality, the stagnation point heat flux should lie somewhere between the equilibrium and frozen estimates. A complete approach to equilibrium is perhaps unlikely due to the short length scales involved.

Table 3: Sutton-Graves stagnation point heat flux predictions for the two types of satellite demise models. The equilibrium and frozen assumptions give the extreme heat fluxes.

Model	**Stag. point heat flux (MW m^{-2})**	
	Equilibrium gas	Frozen gas
Axial	8.93	3.64
Crossflow	23.44	9.56

3.2. Numerical simulations

In order to model heat flux away from the stagnation point, it is necessary to move to two-dimensional computational fluid dynamics (CFD) simulations. Eilmer4 is an open-source Reynolds-averaged Navier–Stokes CFD solver, with the capability to simulate reacting hypersonic flows [7]. Eilmer can act as an equilibrium, chemical non-equilibrium or thermo-chemical non-equilibrium solver depending on the gas model chosen.

Eilmer was used to simulate the axial flow cylinder case. Figure 9 is a temperature plot obtained from Eilmer which shows the mesh used for the axisymmetric heat flux simulations. The well defined T6s312 flow condition was used to set up the CFD. Freestream properties including gas composition were determined using the experimental PITOT output and online CEA2. At the wall, a no-slip fixed temperature boundary condition was applied with a wall temperature of 300 K. This is the standard wall boundary condition for CFD simulations of short-duration T6 test flows. The implied assumption is that there is a step change in heat flux when the test gas arrives, with the wall remaining at constant temper-

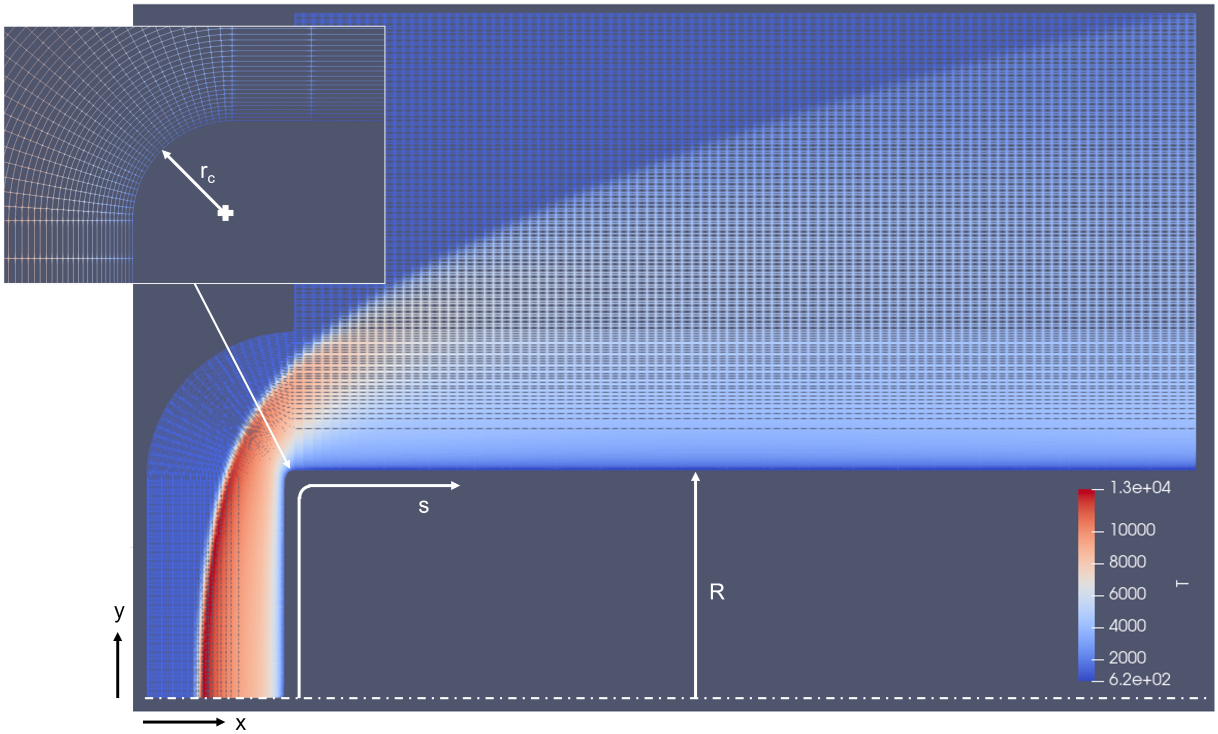

Fig. 9: Temperature plot obtained from Eilmer CFD for an axial cylinder in the T6s312 flow condition with a non-catalytic 300 K no-slip boundary condition applied at the wall. The simulation is dimensionally matched to experiment.

ature throughout the test time [19]. Both a non-catalytic and fully catalytic wall boundary condition were used.

A one-temperature finite rate reaction model was used to simulate thermodynamic equilibrium with chemical non-equilibrium. The gas model implemented was the 11-species reacting air model from Gupta et al. [20], which was developed with hypersonic Earth re-entry flows in mind. A mesh refinement study demonstrated that a mesh density of $1/n_{cells}$ = 3.5x10^{-5} gave a good balance between accuracy and computational cost. Clustering was used towards the wall and stagnation line to fully capture the thermochemistry in these regions.

The stagnation point heat fluxes predicted by Eilmer are 5.6 and 5.4 MW/m^2 for the non-catalytic and catalytic cases, respectively. These values are within the boundaries predicted by the Sutton-Graves correlation with frozen and equilibrium assumptions. The heat flux profiles produced by the Eilmer CFD are shown in Figure 10. Maximum heat flux occurs at the body corner, with the peak heat flux reaching over 1.6 times the stagnation heating for the non-catalytic case. Eilmer predicts that wall catalysis does not have a significant effect on the surface heat flux at this flow condition. The non-catalytic simulation reached a maximum heat flux of 9 MW/m^2, while the fully catalytic simulation reached 8 MW/m^2. This, and the relatively low stagnation point heat fluxes predicted, indicate that the reactions do not have time to progress significantly far towards equilibrium in the shock layer.

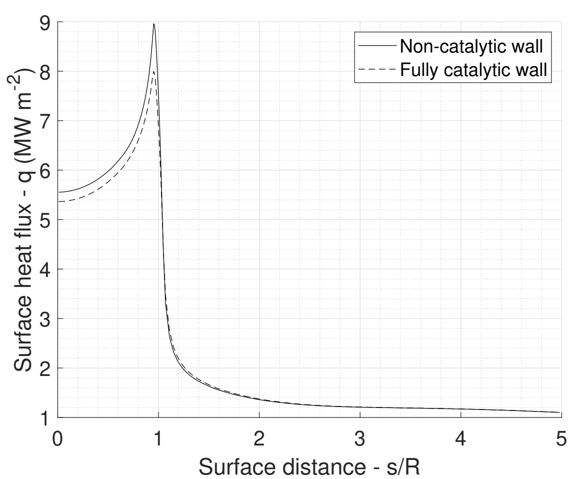

Fig. 10: Heat flux profiles produced using Eilmer CFD for an axial cylinder model in the T6s312 flow condition.

The stagnation pressure and post-shock density obtained from the CFD simulations are well matched to the experimental values seen in the T6s312 test. The post-shock ρL agrees between the CFD and experimental PITOT to within 7%, indicating that the CFD resolves the flowfield fairly well.

Table 4: Flow condition and heat transfer data from the heat flux experiments.

Shot	U_{eq} (m s^{-1})	Post-shock ρL (kg m^{-2})	$\dot{q}$ (model) (MW m^{-2})
T6s336	6543	7.50x10^{-5}	2.32 (A2)
T6s345	6270	1.25x10^{-4}	3.04 (A2) 12.87 (C2)
T6s346	6227	1.17x10^{-4}	17.86 (A1) 6.49 (C1)

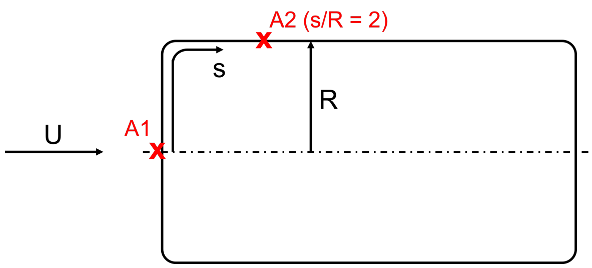

(a) Axial model - side view

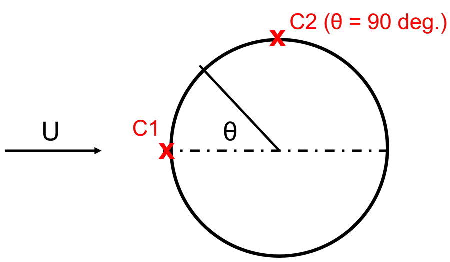

(b) Crossflow model - side view

Fig. 11: Sketches of the models that successfully recorded heat flux measurements, with the gauge positions identified.

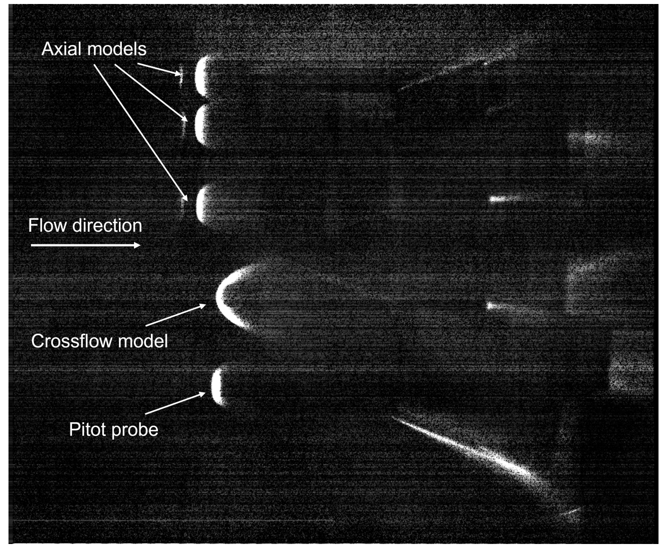

Fig. 12: An image of the experimental setup from shot T6s346, taken during driver gas arrival. Four satellite models were used but two of the axial models failed to record a clean signal.

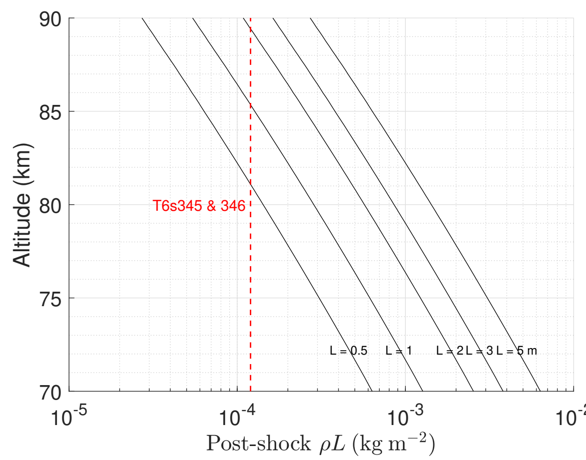

Fig. 13: Matching of post-shock ρL from the heat flux experiments to flight trajectories of cylinders re-entering at 6250 m/s.

4. EXPERIMENTAL RESULTS

The T6 shots performed during the heat transfer experiments are listed in Table 4. At least one satellite model was included in each shot but some failed to capture usable data. This was mostly due to unexpectedly high heat fluxes exceeding the Lancaster voltage limit. Heat fluxes provided in Table 4 are for models where the TFG performed well and a clean signal was recorded. The model type is given alongside the heat flux, with the gauge position of each model type given in Figure 11. A single Pitot probe was also included in each test to provide data on the flow condition and to assist in determining the test time. A photograph of the experimental setup taken during shot T6s346 using a Kirana high speed camera is shown in Figure 12.

Post-shock ρL and flight-equivalent velocity were calculated using the post-processing procedure described in Section 2.1. The PITOT code agrees closely with measured values for shots T6s345 and T6s346, within 4%. However, for shot T6s336 the PITOT code underpredicts Pitot pressure by 28%. This indicates there is likely some error in other PITOT parameters calculated for this test, such as post-shock ρL. It can be seen from the flow parameters in Table 4 that the flow condition of T6s312 could not be exactly replicated in each test. This was due to slight variations in the shock and acceleration tube fill pressures.

The thin film gauges were found to have perished or been severely damaged during each of the tests. Incidents of diaphragm particle collisions with the Macor models were evident, but it is unlikely that these particles caused the destruc-

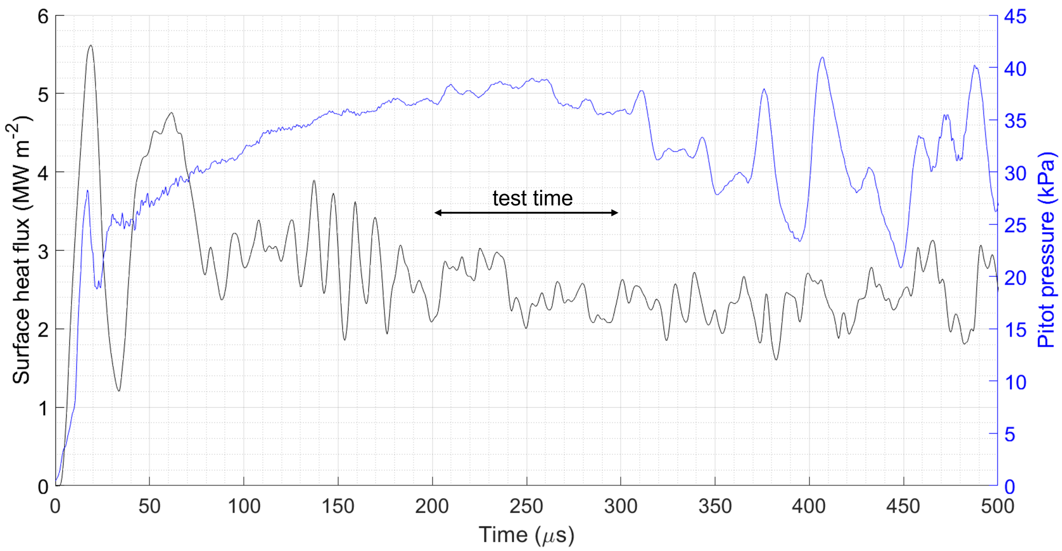

Fig. 14: Data from the sensors used in the T6s336 test. A quasi-steady test time is identified with the assistance of the Pitot probe.

tion of every gauge. The gauges generally appeared visually intact but read as open circuit across the platinum. It is therefore likely that the gauges failed due to the high enthalpy driver gas degrading the platinum. Destruction of the gauges represents a large problem due to the material and labour costs of their construction, but heat transfer data could be gathered before their destruction in most cases. However, if the gauge is degraded gradually, the temperature response of the gauge could be changing throughout the test time. The gauges could also not be re-calibrated after testing to see how their response had changed.

Figure 13 was produced through flight analysis performed at a flight velocity of 6250 m/s, equal to the U_{eq} value from shots T6s345 and T6s346. The post-shock conditions achieved in T6s345 and T6s346 are matched to a range of altitude-diameter combinations within the useful region identified in Figure 2. T6s336 represents a slightly faster, higher altitude test condition. This condition is closer to the targeted U_{eq} value of 7 km/s, but the post-shock ρL is at the upper limit of the useful range, indicating a very high matched altitude.

4.1. Axial cylinder results

Two types of axial cylinder models were successfully tested. The A1 model in shot T6s346 had a gauge at the stagnation point (s/R = 0), while the A2 models used in shots T6s336 and T6s345 had gauges on the side face, 5 mm downstream of the body corner (s/R = 2). Figure 14 shows the sensor data for shot T6s336, with the test time identified.

The heat flux traces obtained from the three axial cylinder models are plotted together in Figure 15. The data from shot T6s346 was particularly noisy, but a quasi-steady test time can still be identified. The heat flux traces have been normalised to rise at $t = 0$ and a similar duration of flow establishment can be seen between tests.

The stagnation point heat flux from test T6s346 of 17.86 MW/m^2 is significantly higher than that predicted by the Eilmer CFD. It is also well beyond the upper limit of heat flux predicted by the Sutton-Graves correlation, 8.93 MW/m^2. Figure 16 plots the experimentally measured heat fluxes against the Eilmer and Sutton-Graves predictions. It can be seen that the off-stagnation A2 gauges also record a much higher heat flux than predicted by Eilmer. The gauge signals appear physical so the implication is that the heat flux at this condition is considerably higher than predicted. This could be due to thermochemical non-equilibrium effects that aren't captured by the one-temperature reaction model used in Eilmer.

Although the condition does vary slightly between T6s345, T6s346 and T6s312 (which was used to setup the CFD), the small variations in U_{eq} and post-shock ρL are not enough to cause such large discrepancies in heat transfer. The post-shock ρL in shot T6s345 was 67% higher than in T6s336. The effect of this was a 32% increase in the heat flux measured by the nominally identical A2 gauges. This further supports the legitimacy of the heat flux measurements but more models should be tested during a single shot for further verification.

4.2. Crossflow cylinder results

Two of the crossflow models successfully recorded heat transfer data. The C1 model tested in T6s346 had a gauge located on the stagnation point, while the C2 model in T6s345 had a

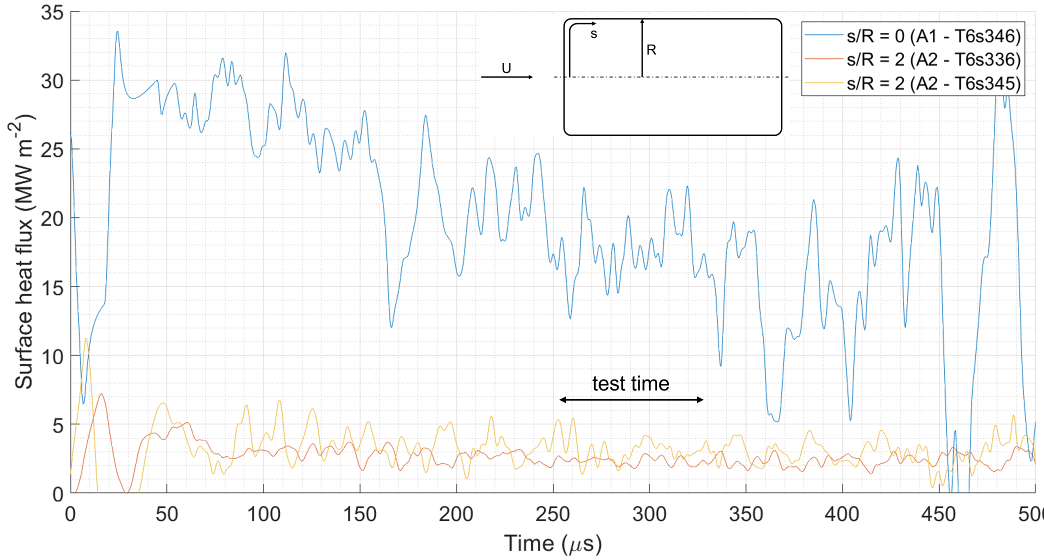

Fig. 15: Heat flux data obtained from the axial cylinder models during the heat flux experiments, with the test time identified.

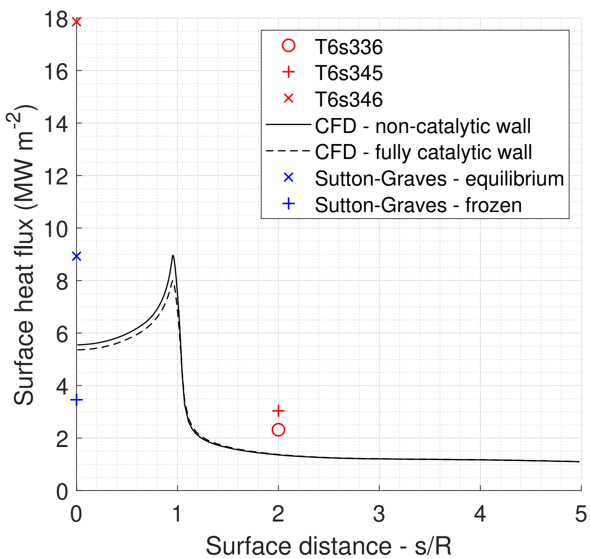

Fig. 16: Experimental heat flux data for the axial cylinder models plotted against predictions from Eilmer CFD and the Sutton-Graves correlation.

gauge located 90 degrees from the stagnation point around the cylindrical face. The heat flux traces for the crossflow gauges are displayed in Figure 17. The test time averaged heat flux measured at the stagnation point was 6.49 MW/m^2 which is 32% lower than the lower bound estimate predicted using the frozen gas assumption in the Sutton-Graves correlation. The off-stagnation C2 gauge actually recorded a heat flux that was almost double that seen at the stagnation point.

Given that the axial heat fluxes were all higher then predicted by theory, it seems that the stagnation point crossflow gauge may have been damaged or poorly calibrated, with its lower-than-expected signal. The high heat flux measured by the C2 gauge supports the idea that heating is greater than predicted by theory at this condition. However, due to the limited amount of data available it cannot be confirmed whether the C1 gauge is performing erroneously. The next round of testing should aim to clarify this.

5. CONCLUSION

In this project, a test bed for performing satellite demise heat transfer experiments in a ground test facility has been successfully established. The T6 expansion tunnel has been used to generate flows with a total enthalpy of 20 MJ/kg and flight-equivalent velocities exceeding 6500 m/s were demonstrated in shot T6s336. Freestream Knudsen numbers exceeding 0.01 were consistently generated, indicating a highly rarefied condition for a short duration facility with enthalpy matched to flight. Post-shock ρL values were in the region of 10^{-4} kg/m^2, indicating post-shock conditions that drive heat transfer were matched to those expected in flight at altitudes of 81-90 km.

Multi-model testing enabled by the newly commissioned ring mount was demonstrated successfully in Shots T6s345 and T6s346 which each saw four TFG-equipped models and a Pitot probe used. Heat transfer data was obtained in shots T6s336, T6s345 and T6s346 using platinum TFGs with a silicon dioxide coating. Data gathered from five of the TFGs appeared to be of good quality, with a quasi-steady test time clearly identifiable. Heat transfer measurements from the axial cylinder models found the heat fluxes to be significantly

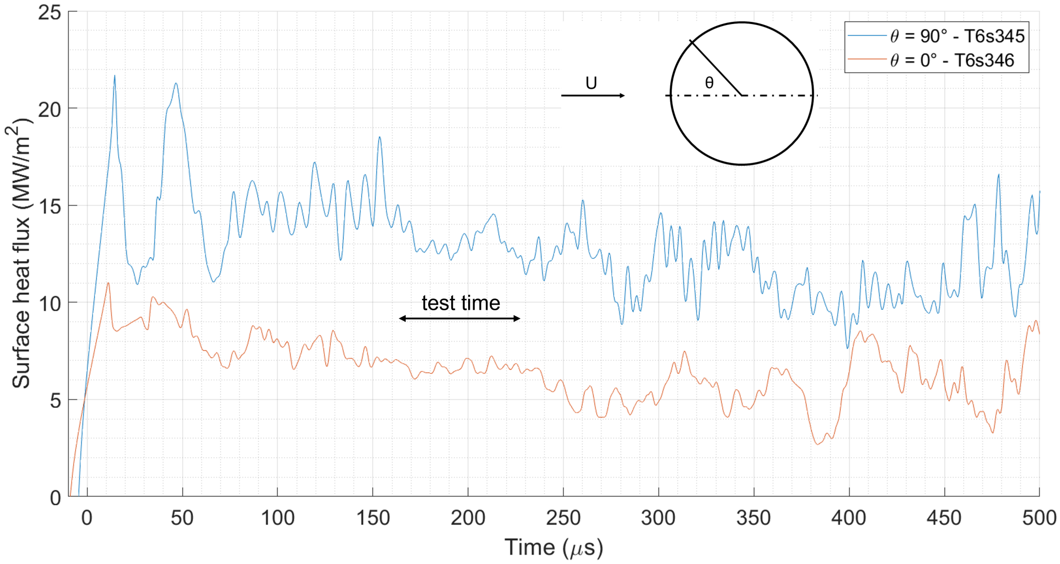

Fig. 17: Heat flux data obtained from the crossflow cylinder models during the heat flux experiments, with the test time identified.

higher than predicted by literature or CFD, with stagnation heating of almost 18 MW/m^2. The crossflow models recorded a high off-stagnation heat flux but a very low heat flux at the stagnation point. There is a clear need for more data to build a better picture of the heat transfer phenomena that are occurring during testing.

In further heat flux testing in the T6 expansion tunnel, it is recommended that the ring mount is used to its full capacity to test more models simultaneously. Testing with one model type only would allow like-for-like comparison of heat flux traces within the same test, verifying that the gauges are behaving physically. This will help determine whether any degradation of the gauges occurs during the test time and provide information on the uniformity of the flow condition. The T6 expansion tunnel can then be used to generate satellite demise datasets at a high altitude LEO re-entry condition.

6. ACKNOWLEDGEMENTS

The contributions of the Oxford Thermofluids Institute Workshop and Instrumentation Lab are greatly appreciated, with particular thanks to Andreea Dabija, Liam Boland and David O'Dell for enabling this project to be completed in time.

7. REFERENCES

[1] Inter-Agency Space Debris Coordination Committee. IADC Space Debris Mitigation Guidelines, IADC-02-01, Revision 2. https://orbitaldebris.jsc.nasa.gov/library/iadc-space-debris-guidelines-revision-2.pdf.

[2] Donald J Kessler and Burton G Cour-Palais. Collision frequency of artificial satellites: The creation of a debris belt. *Journal of Geophysical Research: Space Physics*, 83(A6):2637–2646, 1978.

[3] ESA. Space debris by the numbers. https://www.esa.int/Safety_Security/Space_Debris/Space_debris_by_the_numbers.

[4] The Orbital Debris Program Office. The Orbital Debris Quarterly News, Vol. 6 Issue 2, 2001. https://orbitaldebris.jsc.nasa.gov/quarterly-news/pdfs/odqnv6i2.pdf.

[5] Ronny Kanzler et al. Upgrade of drama's spacecraft entry survival analysis codes. In *7th European Conference on Space Debris (ECSD)*, 2017.

[6] DG Fletcher. Fundamentals of hypersonic flow-aerothermodynamics. *Lecture Series on Critical Technologies for Hypersonic Vehicle Development, Von Karman Institute, Belgium*, pages 10–14, 2004.

[7] Peter Jacobs and Rowan Gollan. Implementation of a compressible-flow simulation code in the d programming language. In *Applied Mechanics and Materials*, volume 846, pages 54–60, 2016.

[8] Matthew Thompson, Christopher M James, Steven W Lewis, David E Gildfind, and Richard G Morgan. Generating 5-km/s low density hypersonic test flows in an

expansion tube for studying ultraviolet radiation. ISSW, 2019.

[9] Peter Collen et al. Development and commissioning of the t6 stalker tunnel. *Experiments in Fluids*, 62(11):1–24, 2021.

[10] Matthew McGilvray, Peter Collen, Luke Doherty, Joseph Steer, James Leader, Alex Glenn, and Chris Hambidge. The oxford t6 stalker tunnel: performance, upgrades and new modes of operation. 2022.

[11] M McGilvray, L Doherty, R Morgan, and D Gildfind. T6: The oxford university stalker tunnel. In *20th AIAA International Space Planes and Hypersonic Systems and Technologies Conference*, July 2016.

[12] Sanford Gordon and Bonnie J McBride. Computer program for calculation of complex chemical equilibrium compositions and applications. part 1: Analysis. Technical report, 1994.

[13] CM James et al. Implementation of a state-to-state analytical framework for the calculation of expansion tube flow properties. *Shock Waves*, 28(2):349–377, 2018.

[14] European Space Agency. Discos (database and information system characterising objects in space).

[15] Klaus Willeke and Daniel Bershader. An improved thin-film gauge for shock-tube thermal studies. *Review of Scientific Instruments*, 44(1):22–25, 1973.

[16] Kenneth Sutton and Randolph A Graves Jr. A general stagnation-point convective heating equation for arbitrary gas mixtures. Technical report, 1971.

[17] Ernest V Zoby and Edward M Sullivan. Effects of corner radius on stagnation-point velocity gradients on blunt axisymmetric bodies. *Journal of Spacecraft and Rockets*, 3(10):1567–1567, 1966.

[18] SL Gai and NR Mudford. Stagnation point heat flux in hypersonic high enthalpy flow. *Shock Waves*, 2(1):43–47, 1992.

[19] JE Doorly and MLG Oldfield. The theory of advanced multi-layer thin film heat transfer gauges. *International journal of heat and mass transfer*, 30(6):1159–1168, 1987.

[20] R Gupta et al. A review of reaction rates and thermodynamic and transport properties for an 11-species air model for chemical and thermal nonequilibrium calculations to 30000 K. https://ntrs.nasa.gov/citations/19900017748, 1990.